

### **OPEN ACCESS**

# Tracking Through-Thickness Dynamics in Lithium–Sulfur Batteries via Operando Raman Imaging and a Purpose-Built Cell

To cite this article: Saeed Yari et al 2025 J. Electrochem. Soc. 172 110520

View the article online for updates and enhancements.

## You may also like

- Physico-Chemical and Electrochemical Analysis of Hard-Carbon From Licorice Root Bio-Waste as Anode for Sodium Ion Batteries

Asia Patriarchi, Leonardo Sbrascini, Jonathan Caroni et al.

- Effect of Ionomer-to-Carbon Ratio on PEMFC Carbon Corrosion: An Electrochemical Study Sebastian Raab, Ayon Karmakar, Po-Ya Abel Chuang et al.

- <u>State of Health Estimation for Lithium-Ion</u>
<u>Batteries Based on Global Feature</u>
<u>Extraction and KPCA-ISSA-LSSVM Model</u>
Xu He, Hainan Wang, Yuan Jiang et al.

# Your Lab in a Box!

The PAT-Tester-i-16 Multi-Channel Potentiostat for Battery Material Testing!

- ✓ All-in-One Solution with Integrated Temperature Chamber (+10 to +80 °C)! No additional devices are required to measure at a stable ambient temperature.
- ✓ Fully Featured Multi-Channel Potentiostat / Galvanostat / EIS!

  Up to 16 independent battery test channels, no multiplexing.
- ✓ Ideally Suited for High-Precision Coulometry! Measure with excellent accuracy and signal-to-noise ratio.
- ✓ Small Footprint, Easy to Setup and Operate! Cableless connection of 3-electrode battery test cells. Powerful EL-Software included.



Learn more on our product website:



Download the data sheet (PDF):



Or contact us directly:

- +49 40 79012-734
- www.el-cell.com





## Tracking Through-Thickness Dynamics in Lithium-Sulfur Batteries via Operando Raman Imaging and a Purpose-Built Cell

Saeed Yari, 1,2,3 Jonathan Buntinx, 1 Martijn Schepers, 1 Albin Conde Reis, 1,2 Thomas Vranken, 1,2,3 Quanquan Pang, 4 An Hardy, 1,2,3 and Mohammadhosein Safari 1,2,3,z

Most existing operando methods lack the spatial resolution or measurement access required for cross-sectional analysis of battery electrodes. Here, we present a custom-designed operando electrochemical cell, enabling real-time, through-thickness investigations. Applied to a lithium-sulfur battery, this setup reveals gradual and spatially non-uniform sulfur utilization, dissolution, and reprecipitation. Depth-resolved measurements indicate highly nonuniform sulfur utilization, with earlier sulfur depletion near the current collector. Accessing the electrode cross-section provides critical insights into reaction heterogeneity and dynamics that are inaccessible via conventional measurements. This offers a deeper understanding of battery behavior and facilitates the design of cells with improved performance and durability.

© 2025 The Author(s). Published on behalf of The Electrochemical Society by IOP Publishing Limited. This is an open access article distributed under the terms of the Creative Commons Attribution 4.0 License (CC BY, https://creativecommons.org/licenses/by/4.0/), which permits unrestricted reuse of the work in any medium, provided the original work is properly cited. [DOI: 10.1149/1945-7111/ae1bde]

Manuscript submitted July 22, 2025; revised manuscript received September 14, 2025. Published November 12, 2025.

Supplementary material for this article is available online

Rechargeable batteries operate through complex electrochemical reactions, ion transport, and phase transformations that evolve dynamically during cycling. These processes are highly transient and spatially heterogeneous within the electrode, creating gradients in composition, conductivity, and mechanical stress that strongly affect performance and degradation of the electrode. Traditional ex situ methods cannot capture such dynamic, spatially resolved behavior, making operando characterization—real-time monitoring under realistic conditions—essential for mechanistic understanding and rational battery design.

The through-thickness direction of battery electrodes is particularly compelling to investigate under operando conditions, as it directly captures the spatial and temporal evolution of electrochemical processes across the most functionally critical axis of the cell.  $^{4.5}$  Tracking reaction dynamics along this axis provides direct insight into gradients in state-of-charge, active material utilization, interfacial phenomena, and transport limitations.  $^{6-9}$ 

Most operando characterization techniques are limited in capturing depth-dependent variations, either probing only the surface or providing bulk-averaged measurements. Techniques like operando X-ray diffraction (XRD) track bulk phase changes but cannot resolve electrode-thickness variations and require X-ray transparent cells made of e.g. beryllium. 10 Nuclear Magnetic Resonance (NMR) provides bulk ion mobility information but lacks spatial resolution.<sup>11</sup> Neutron diffraction can localize lithium but demands complex, neutron-transparent cells and often larger geometries, limiting routine use. <sup>12</sup> X-ray computed tomography (CT) offers 3D imaging of electrode microstructure evolution, but lab-based CT is slow, while synchrotron-based CT requires large-scale facilities and lacks chemical specificity. 13 Surface-sensitive techniques such as Xray photoelectron spectroscopy (XPS), atomic force microscopy (AFM), and electron microscopy deliver high-resolution chemical and morphological detail but are restricted to small volumes, require demanding sample preparation, and operate under strict environmental conditions, making them unsuitable for real-time, throughthickness operando analysis. 14,15

In this work, we present a new Raman operando cell for the visualization of the through-thickness heterogeneity in the battery

porous electrodes and showcase its added value for the study of dynamics of dissolution and precipitation in sulfur electrodes. The operando optical microscopy and Raman spectroscopy offer practical advantages for cross-sectional studies. The spatial resolution and chemical sensitivity of these techniques enables detailed in situ observation of heterogeneities, making them indispensable tools for investigating dynamic processes in battery electrodes. <sup>16</sup> Custom cells optimized for optical access have been successfully demonstrated in earlier studies—for example, Hogrefe et al. <sup>17</sup> designed a setup that allowed direct visualization of color gradients across a graphite electrode in a Li-ion battery, or have used similar cells to monitor copper current-collector dissolution. <sup>18</sup>

#### **Experimental**

Figures 1 and S1 present detailed views of our custom-designed electrochemical cell developed to enable cross-sectional operando microscopy and spectroscopy. Figure 1a shows an expanded schematic of the cell architecture. The system was engineered with key design priorities in mind: flexibility to accommodate a wide range of cell chemistries, adjustable stack pressures; reliable airtight sealing, full exposure of the electrode cross-section, and unobstructed optical access to the active area.

The core component of the cell is a modular PEEK (polyether ether ketone) unit, which houses the electrodes and separators and serves as the site for electrochemical reactions (Fig. 1a, Part I; Fig. 1b). The rest of the cell is made of stainless steel. The interior of the PEEK body features a 15 mm semi-circular cavity designed to accommodate two stainless steel inserts (Fig. 1a, Part II), each with a matching semi-circular cross-section. These inserts have narrow extensions that slide into corresponding grooves in the PEEK body and connect to electrical wiring, functioning as current collectors. Electrodes and separators are carefully cut in half and positioned between the inserts, with one insert fixed at the end of the PEEK holder and the other movable. The inserts are brought together, leaving a small gap for liquid electrolyte addition. Once the electrolyte is added, full compression is applied using a screwdriven spring (Fig. 1a, Part III), completing the PEEK assembly. The assembled PEEK body is placed into the bottom stainless steel compartment with electrical connections (Fig. 1a, Part IV; Fig. 1c). Finally, the top stainless steel compartment, featuring a sapphire

<sup>&</sup>lt;sup>1</sup>Institute for Materials Research (IMO-imomec), UHasselt, Hasselt, 3500, Belgium

<sup>&</sup>lt;sup>2</sup>Energyville, Thor Park 8320, Genk 3600, Belgium

<sup>&</sup>lt;sup>3</sup>IMEC Division IMOMEC, Diepenbeek 3590, Belgium

<sup>&</sup>lt;sup>4</sup>Beijing Key Laboratory for Theory and Technology of Advanced Battery Materials, School of Materials Science and Engineering, Peking University, Beijing 100871, People's Republic of China

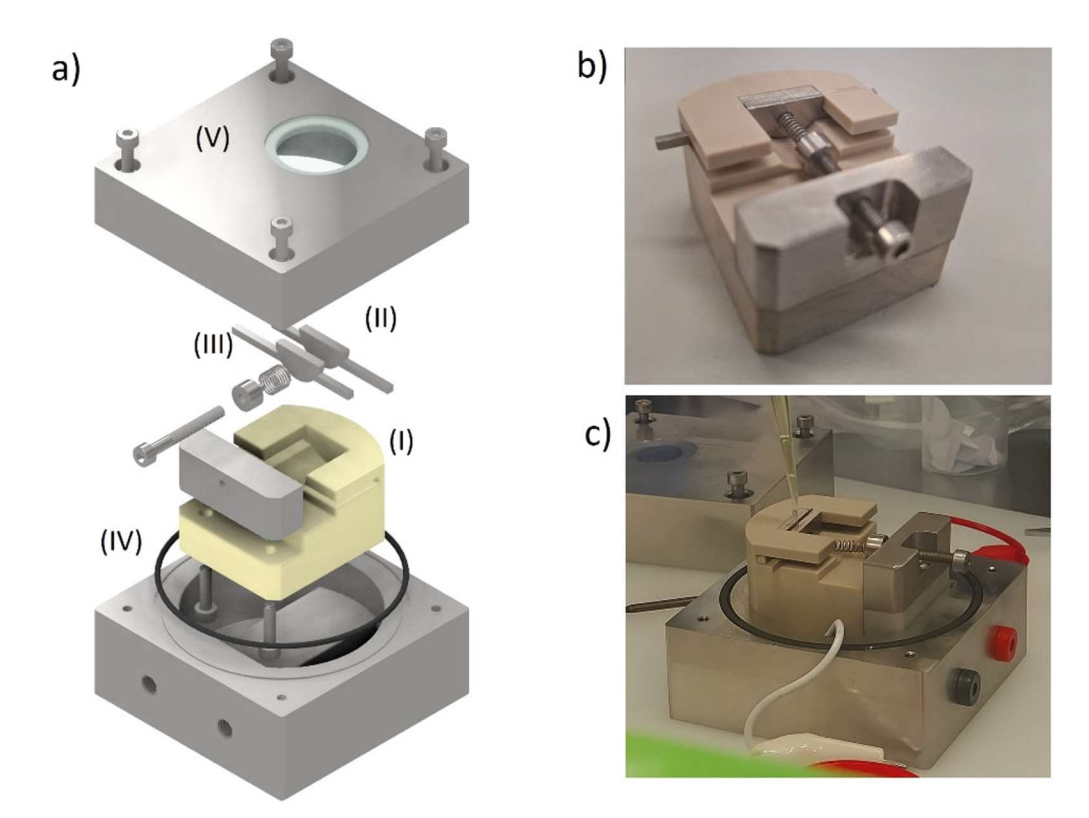


**Figure 1.** (a) Expanded view of the cell architecture. *Part II:* PEEK body, *Part III:* Stainless-steel sliders serving as the current collectors, *Part III:* compression mechanism, Part IV: bottom holder with electric connections, *Part V:* cell enclosure with optical access, (b) The PEEK body serving as the main housing for the electrochemical reaction, featuring a 15 mm diameter circular cavity for semi-circular electrodes. (c) Cell assembly inside the glovebox, showing electrolyte addition between the stainless steel inserts, where the electrodes are aligned.

window, is positioned and sealed with an O-ring (Fig. 1a, Part V), providing optical access. All assembly steps are carried out inside an argon-filled glovebox. The modular design of the cell enables operando measurements across a range of chemistries, including Li-ion, Na-ion, and Li–S systems. Its architecture is specifically optimized for compatibility with confocal Raman microscopy, optical microscopy, in situ UV–vis and fluorescence imaging, allowing spatially resolved characterization of electrochemical processes in real time, at the electrode cross section.

The operando cell was used for the Raman microscopy on the cross-section of a Li–S cell employing a sulfur cathode composed of 70 wt% sulfur, 20 wt% carbon black, and 10 wt% PVDF binder, a thin Li metal anode, and 150  $\mu l$  of electrolyte. Raman spectroscopy was performed using a confocal Raman microscope (Renishaw inVia^TM) equipped with a 532 nm excitation laser, and a motorized XYZ stage for precise spatial mapping. Initially, the electrode cross-section was examined under optical microscopy to identify regions of interest exhibiting morphological features indicative of sulfur particles. Subsequent point Raman measurements were conducted to confirm the presence of sulfur in these regions.

### **Results and Discussion**

To demonstrate the value of our in situ cell, we performed operando measurements on a lithium–sulfur (Li–S) battery. Li–S cells operate via a conversion chemistry involving the formation and dissolution of polysulfides and the precipitation of insulating lithium sulfide.  $^{19,20}$  Sulfur is well-suited for Raman analysis due to its strong scattering and the high polarizability of S–S bonds. Elemental sulfur, particularly  $S_8$  rings, exhibits intense, well-defined Raman-active vibrational modes, enabling clear identification of sulfur and lithium polysulfide intermediates.  $^{15,21,22}$  Thus, Raman spectroscopy offers a powerful, non-destructive method to monitor chemical speciation and phase transformations during electrochemical cycling in Li–S systems.

A representative discharge profile of a Li-S battery is shown in Fig. S2. In cells utilizing conventional ether-based electrolytes—specifically, 1 M lithium bis(trifluoromethanesulfonyl)imide (LiTFSI), 1 wt% LiNO3, dissolved in a 1:1 volume ratio of 1,3-dioxolane (DOL) and dimethoxyethane (DME)—the discharge process can be broadly divided into two distinct stages. During the first stage, elemental sulfur (S8, solid) is reduced to soluble long-chain polysulfides, progressing sequentially from S8 to Li2S6 and Li2S4. The second stage involves further reduction of these soluble intermediates to insoluble shortchain polysulfides and ultimately to solid discharge products, including Li2S2 and Li2S1  $^{19}$ 

Figure 2 presents operando Raman microscopy of the cross-section of a selected area of approximately  $40\times100\,\mu\text{m}^2$  (step size of  $2\,\mu\text{m}$  in each direction) on the sulfur cathode, encompassing a few large sulfur particles (Fig. 2a). In order to simplify the investigation of the sulfur dissolution and precipitation dynamics, the measurements were limited to a shallow discharge and charge cycle, i.e. part I in (dis)charge profile (Fig. S2). Raman spectra were collected at discrete 20 min intervals during discharge (Fig. 2b), followed by a final mapping after a full charge cycle via a constant current-constant voltage (CC-CV) protocol, in order to assess the reappearance and spatial redistribution of sulfur particles.

Figure S3 shows representative Raman spectra averaged over the entire scanned area at various stages of discharge. At the onset of discharge, the spectra are dominated by characteristic peaks of elemental sulfur (S<sub>8</sub>) located near 150, 220, and 470 cm<sup>-1</sup>. These sulfur peaks gradually shrink over discharge, while two new bands emerge at 400 and 430 cm<sup>-1</sup>, corresponding to long-chain (Li<sub>2</sub>S<sub>6</sub>) and short-chain (Li<sub>2</sub>S<sub>4</sub>) lithium polysulfides, respectively.<sup>23</sup> Complementary Raman maps (Figs. 2c–2i) reveal the spatial evolution of sulfur, where bright regions indicate sulfur-rich areas and dark regions correspond to the carbon-binder domains and pore volume. A progressive loss of sulfur signal is observed, and by 2.18 V, sulfur particles have completely disappeared. Upon full

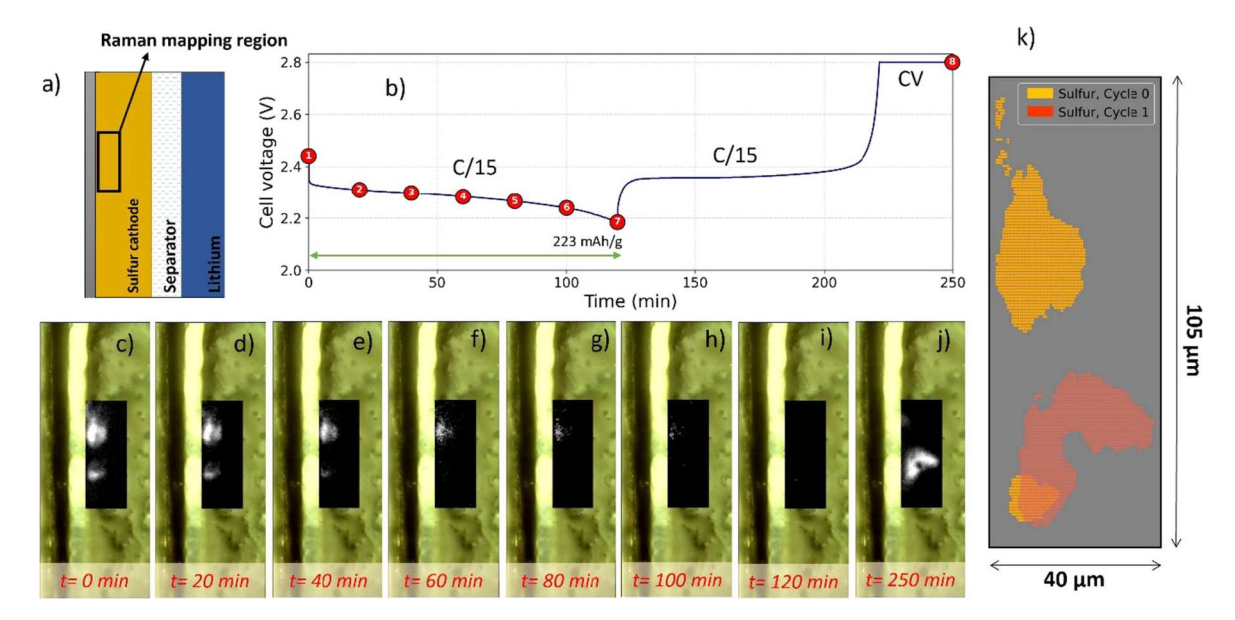


Figure 2. (a) The selected area for Raman mapping across the full through-thickness of the cell. (b) Voltage–time profile of a Li–S cell during a shallow cycle, indicating the time intervals at which Raman measurements were recorded. (c–i) Raman maps of sulfur over an area of  $\sim 40 \times 100 \ \mu m^2$  of the cathode, overlaid on corresponding microscopy images, at various time points from 0 to 120 min into discharge. *Greenish region*: optical image of the cross section, *Black region*: selected area for Raman mapping, *white shade*: identified sulfur. (j) Raman map after a full charge, i.e. at 250 min. (k) 2D reconstruction of sulfur particles showing their redistribution to different locations after one cycle.

recharge, sulfur reappears (Fig. 2j), though with altered morphology and spatial distribution—a process better visualized in Fig. 2k.

This redistribution of sulfur originates from the dissolution and mobility of lithium polysulfides during discharge, allowing them to move away from their initial locations.<sup>24</sup> During charge, these species precipitate back as solid sulfur, but often in new positions and with modified morphology due to the complex interplay among reaction pathways, electrolyte composition, and cathode structure. Such sulfur redistribution is often accompanied by a decrease in sulfur utilization and capacity retention.<sup>25,26</sup>

The sulfur solubility and polysulfides mobility are very sensitive to the electrolyte system. For instance, the sparingly solvating electrolytes (SSEs)—including high-concentration and hydrofluor-oether-based systems—suppress the polysulfide dissolution. In contrast, highly solvating electrolytes (HSEs) with high donor number solvents enhance polysulfide solubility. Our operando system provides a powerful diagnostic tool to visualize and study the dissolution and redistribution dynamics of sulfur in different electrolyte formulations.

A second operando Raman experiment was conducted to study the full cross-section of the sulfur cathode, encompassing an area of  $85 \times 270 \,\mu\text{m}^2$  (4  $\mu$ m step size), as shown in Fig. 3a. Operando Raman spectra were recorded during a shallow discharge over 100 min at C/20 rate, with data collected at discrete 20 min intervals (Fig. 3b). The corresponding Raman spectra and spatial maps are presented in Figs. S4 and 3c-3h, respectively. Sulfur (white shade) is observed to be distributed throughout the electrode thickness, appearing near the current collector, in the mid-region, and at the electrode surface. Upon the onset of discharge, sulfur dissolution is evidenced by the progressive reduction in white pixels across the Raman maps. To quantify this behavior, we analyzed the spatial distribution of sulfur-related pixels across the electrode thickness over time, as shown in Figs. 3i-3n. Each peak corresponds to sulfur particles located at different distances from the current collector, and their gradual decrease in intensity reflects sulfur dissolution.

The depth-resolved measurements suggest highly non-uniform sulfur utilization across the electrode thickness. From 0 to 20 min, the two largest peaks below 40  $\mu m$  shrink the most, while between 20 and

40 min, the peak near  $60~\mu m$  is most affected. Between 40 and 60 min, dissolution slows down with minimal changes. From 60 to 80 min, the peaks around  $60~\mu m$  shrink noticeably. By the end of the 100 min discharge, the peak below  $20~\mu m$  disappears completely, while the peak near  $80~\mu m$  still persists, suggesting possible delayed sulfur utilization near the electrode surface and relatively faster conversion closer to the current collector. The peak near  $80~\mu m$  also shows a brief intensity increase at around 80~min; however, this is likely an artifact caused by electrode shrinkage temporarily shifting a particle initially outside the scanned region into the measurement area. These dissolution patterns may also reflect variations in sulfur particle size and distribution across the electrode thickness. Smaller sulfur particles tend to dissolve more quickly, while larger particles may persist longer.

Our observation deviates from commonly reported trends for optimized porous electrodes in Li-ion batteries, where utilization near the current collector usually lags behind that closer to the separator. Through physics-based simulations, <sup>28</sup> neutron diffraction probing of lithium distribution across electrode depth, <sup>7</sup> and specialized electrochemical setups, <sup>29,30</sup> it has been demonstrated that ion transport limitations in the electrolyte typically outweigh the electronic resistance in the solid matrix, resulting in preferential reaction near the separator side.

Our operando results reveal nonuniform utilization across the sulfur electrode, without a sharp or continuous gradient, but with a tendency for earlier sulfur depletion near the current collector, suggesting a more effective ionic and electronic percolation network in that region. This also implies a higher likelihood of Li<sub>2</sub>S deposition at the current collector interface which can lead to a premature end of discharge, also reported by Reis et al.<sup>31</sup> In this regard, the use of a through-thickness operando system can facilitate the rational design of improved electrode architectures. For instance, introducing a gradient in composition or porosity—such as enhancing ionic conductivity or electrolyte access near the current collector, or optimizing carbon content across the thickness-and deliberately leveraging constructive heterogeneity can help balance reaction kinetics throughout the electrode, 32,33 promoting more uniform sulfur utilization, and ultimately extending the cycle life of Li-S batteries.

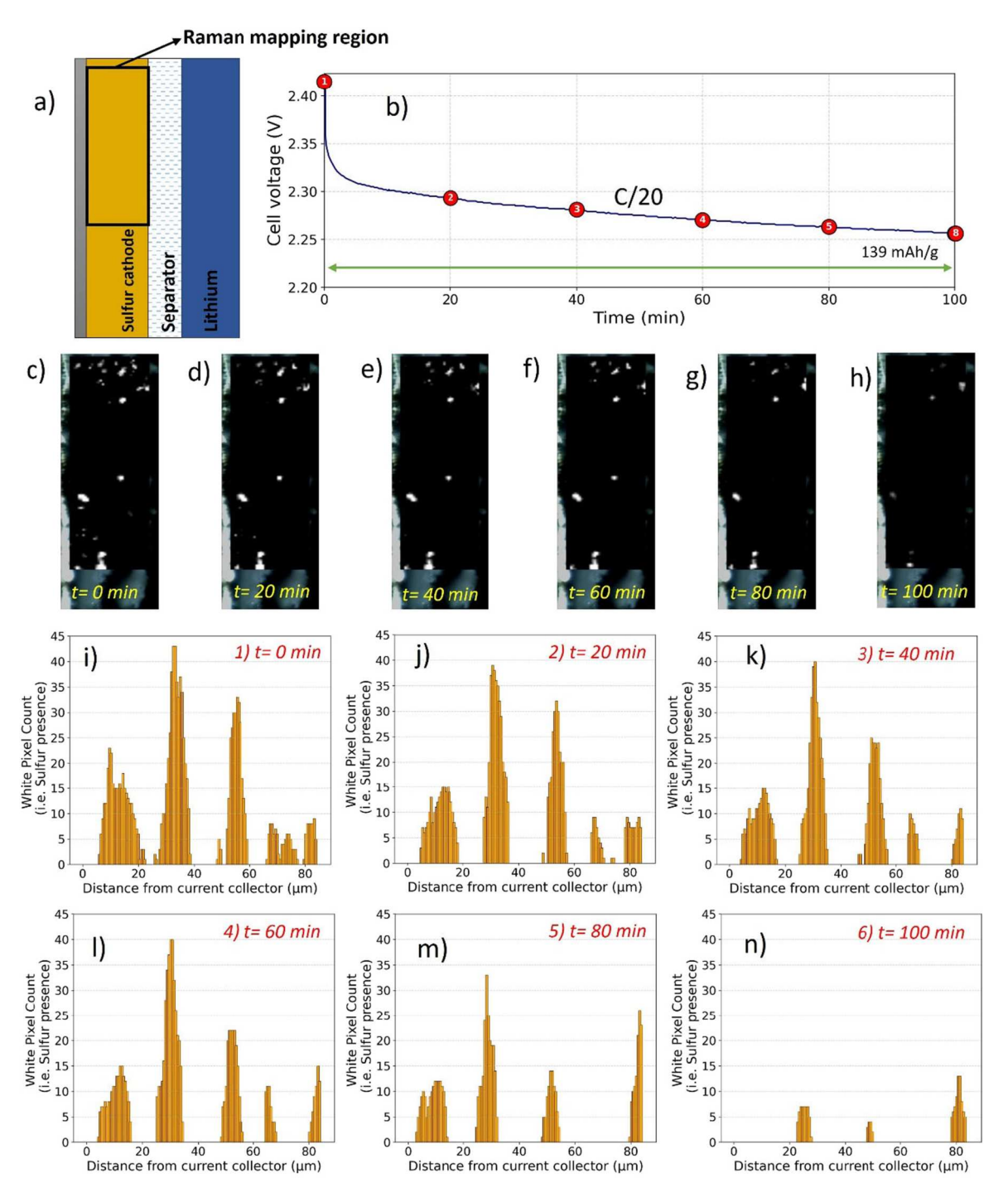


Figure 3. (a) The selected area for Raman mapping across the full through-thickness of the cell. (b) Voltage–time profile of a Li–S cell during a shallow cycle, indicating the time intervals at which Raman measurements were performed. (c)–(h) Raman maps of sulfur over the entire cross section of the cathode, overlaid on corresponding microscopy images, at various time points from 0 to 100 min into discharge. White pixels indicate sulfur. (i)–(n) Sulfur-related pixel count as a function of distance from the current collector, illustrating the spatially resolved sulfur dissolution across the cathode. Each peak corresponds to sulfur particles located at different distances from the current collector.

#### Conclusions

This work introduces an operando Raman microscopy approach tailored to visualize cross section of a lithium–sulfur cell, enabled by a custom-designed cell architecture. Real-time Raman mapping revealed significant sulfur redistribution upon cycling, with sulfur reappearing in altered locations and morphologies after recharge. Furthermore, depth-resolved sulfur dissolution showed earlier sulfur depletion near the current collector. These findings highlight the value of operando, cross-sectional techniques in uncovering depth-

dependent dynamics of charge/discharge in battery porous electrodes. The methodology presented here offers a versatile diagnostic platform for guiding rational electrode and electrolyte design across diverse battery chemistries.

#### Acknowledgments

This work was supported by SIM (Strategic Initiative Materials in Flanders) and VLAIO (Flemish Government Agency Flanders Innovation and Entrepreneurship) within the SBO project "FuGels"

(Grant HBC.2021.0016) under the SIM research program "SIMBA –Sustainable and Innovative Materials for Batteries.'

#### ORCID

Mohammadhosein Safari https://orcid.org/0000-0003-0633-731X

#### References

- 1. H. Du et al., Advanced Mater., 36, 2401482 (2024).
- 2. C. D. Quilty, D. Wu, W. Li, D. C. Bock, L. Wang, L. M. Housel, A. Abraham, K. J. Takeuchi, A. C. Marschilok, and E. S. Takeuchi, Chem. Rev., 123, 1327 (2023).
- 3. D. Liu et al., Adv. Mater., 31, 1806620 (2019).
- 4. C. Niu et al., Nat. Energy, 6, 723 (2021).
- 5. X. Lu et al., Nat. Commun., 11, 2079 (2020).
- S. J. Harris and P. Lu, *J. Phys. Chem. C*, **117**, 6481 (2013).
   H. Zhou, K. An, S. Allu, S. Pannala, J. Li, H. Z. Bilheux, S. K. Martha, and J. Nanda,, ACS Energy Lett., 1, 981 (2016).
- 8. H. Gao, Q. Wu, Y. Hu, J. P. Zheng, K. Amine, and Z. Chen, J. Phys. Chem. Lett., 9, 5100 (2018).
- 9. B. K. Cho, S. Y. Jung, S. J. Park, J. H. Hyun, and S. H. Yu, ACS Energy Lett., 9, 4068 (2024).
- 10. G. Gourdin and V. Doan-Nguyen, Cell Reports Phys. Sci., 2, 100660 (2021).
- 11. S. Castelletto and A. Boretti, Mater. Today Energy, 31, 101210 (2023).
- 12. S. Wang, H. Shi, D. Wang, Y. Xia, Y. Yin, S. Liang, Y. Hu, R. Shao, X. Wu, and Z. Xu, Nano Energy, 122, 109337 (2024).
- 13. F. Tang et al., Small Methods, 5, 2100557 (2021).
- 14. I. Kallquist, R. L. Ruyet, H. Liu, R. Mogensen, M.-T. Lee, K. Edstrom, and A. J. Naylor, J. Mater. Chem. A, 10, 19466 (2022).
- 15. H. Yang, P. Tang, N. Piao, J. Li, X. Shan, K. Tai, J. Tan, H.-M. Cheng, and F. Li, Mater. Today, 57, 279 (2022).

- 16. Z. Deng, X. Lin, Z. Huang, J. Meng, Y. Zhong, G. Ma, Y. Zhou, Y. Shen, H. Ding, and Y. Huang, Advanced Energy Materials, 11, 2000806 (2021).
- 17. C. Hogrefe, T. Waldmann, M. B. Molinero, L. Wildner, P. Axmann, and M. Wohlfahrt-Mehrens, J. Electrochem. Soc., 169, 050519 (2022).
- 18. J. Kuwabara and K. Sato, ECS Trans., 75, 47 (2017).
- 19. H. Raza, S. Bai, J. Cheng, S. Majumder, H. Zhu, Q. Liu, G. Zheng, X. Li, and G. Chen, Electrochem. Energy Rev., 6, 29 (2023).
- 20. S. Yari, A. C. Reis, Q. Pang, and M. Safari, Nat. Commun., 16, 5473 (2025).
- 21. B. A. Trofimov, L. M. Sinegovskaya, and N. K. Gusarova, J. Sulfur Chem., 30, 518 (2009)
- 22. L. Xue et al., Small Struct., 3, 2100170 (2022).
- 23. S. Lang, S. H. Yu, X. Feng, M. R. Krumov, and H. D. Abruña, Nat. Commun., 13, 4811 (2022)
- 24. P. Strubel, S. Thieme, C. Weller, H. Althues, and S. Kaskel, Nano Energy, 34, 437 (2017).
- 25. D. Di Lecce, V. Marangon, W. Du, D. J. L. Brett, P. R. Shearing, and J. Hassoun, J. Power Sources, 472, 228424 (2020).
- 26. L. Kong, Q. Jin, J. Q. Huang, L. D. Zhao, P. Li, B. Q. Li, H. J. Peng, X. Zhang, and Q. Zhang, *Energy Technol.*, 7, 1900111 (2019).
- 27. Y. Liu, Y. Elias, J. Meng, D. Aurbach, R. Zou, D. Xia, and Q. Pang, Joule, 5, 2323 (2021).
- 28. S. Malifarge, B. Delobel, and C. Delacourt, J. Electrochem. Soc., 165, A1275 (2018).
- 29. S. Klink, W. Schuhmann, and F. La Mantia, ChemSusChem, 7, 2159 (2014).
- 30. T. Sasaki, C. Villevieille, Y. Takeuchi, and P. Novák, Adv. Sci., 2, 2 (2015).
- 31. A. C. Reis, S. Yari, J. D'Haen, A. Hardy, N. Reddy, and M. Safari, Batter. Supercaps, 6, e202300286 (2023).
- 32. S. Yari, H. Hamed, J. D'Haen, M. K. Van Bael, F. U. Renner, A. Hardy, and M. Safari, ACS Appl. Energy Mater., 3, 11820 (2020).
- 33. H. Xu, J. Zhu, D. P. Finegan, H. Zhao, X. Lu, W. Li, N. Hoffman, A. Bertei, P. Shearing, and M. Z. Bazant, Adv. Energy Mater., 11, 2003908 (2021).